

Magnetic Fabry-Pérot interferometer for valley filtering in a honeycomb-dice model

F. Bouhadida, L. Mandhour, and S. Charfi-Kaddour

Laboratoire de Physique de la Matière Condensée,

Département de Physique, Faculté des Sciences de Tunis,

Université Tunis El Manar, Campus Universitaire 1060 Tunis, Tunisia

(Dated: March 20, 2020)

Here we theoretically investigate the valley-dependent transmission of particles through a combined electric and magnetic barrier in the $\alpha - T_3$ model which interpolates between the honeycomb and the dice lattices. We put forward that the combination of the Fabry-Pérot interferences and the magnetic field leads to a perfect transmission for one valley and a suppression of the transmission for the other valley. When only one of the barriers (magnetic or electric) is present, no valley polarized current can be produced. By tuning the Fermi energy, this valley-dependent peculiar behavior can be used as valley filtering. Our results show that highly efficient valley filtering with maximum conductivity and polarization can be achieved by controlling the value of the magnetic field and the electric barrier width and height.

I. INTRODUCTION

The *valley* degree of freedom in condensed matter materials opened the door to a new field referred as *valleytronics*^{1,2} which is reminiscent of the spintronics³. The band structure of the valleytronics materials must have at least two inequivalent valleys in order to control the current coming from each valley. Graphene, a single sheet of carbon atoms arranged in a honeycomb lattice (HCL) that offers two *valleys* K and K' , is one of the most used valleytronics materials. In the existing literature different methods to obtain a valley filter in graphene have been presented such as lattice strain⁴⁻⁸, line defect^{9,10}, trigonal warping effect¹¹, the effect of mirror-symmetry breaking¹² and strong electrostatic potential¹³. The black phosphorus has also been used as valley filter with the merging of Dirac cones¹⁴. As well, the presence of a magnetic field and a potential barrier in bilayer graphene acts as a valley filter¹⁵.

Raoux *et al.*¹⁶ introduced the $\alpha - T_3$ model that is obtained from a HCL by adding in the center of each hexagon an extra site related to one of the sites A or B by an α -dependent hopping amplitude that adjusts the coupling between atoms. The interest of the $\alpha - T_3$ model lies in the fact that it interpolates via the parameter α between graphene ($\alpha = 0$) and dice lattice (or T_3)^{17,18} ($\alpha = 1$) and that its energy spectrum does not depend on α . It has been showed that $Hg_{1-x}Cd_xTe$ ¹⁹ for a critical value $x = 0.17$, maps onto the $\alpha - T_3$ structure for a parameter $\alpha = \frac{1}{\sqrt{3}}$. The energy band spectrum of the $\alpha - T_3$ model is composed of two dispersive bands similar to those of graphene and a dispersionless flat band that crosses the K and K' valleys. One of the most striking characteristics for the $\alpha - T_3$ model is that the dispersion relation at low energy is linear and the particles behave as massless Dirac particles with a hybrid pseudospin that is an admixture of pseudospin $S = 1/2$ of graphene and pseudospin $S = 1$ of dice lattice. As a consequence, many unusual properties have been attributed to the $\alpha - T_3$ model such as Klein tunneling²⁰ that consists in perfect transmission across a potential barrier that occurs at nor-

mal incidence and it is related to the conservation of the pseudospin²¹. Perfect transmission at oblique incidence can arise from Fabry-Pérot interferences of the particle bouncing between the two interfaces of the barrier for all values of α ²¹. For the dice lattice, when the energy of the incident particle is equal to half of the barrier height, a peculiar property called super Klein tunneling²² is observed. It corresponds to the perfect transmission of the particles through the barrier for all the incidence angles. It has been demonstrated that inhomogeneous magnetic field can suppress the Klein tunneling²³ and confine particles in graphene²⁴ and dice lattice²². Another significant property of the $\alpha - T_3$ model is that when a perpendicular magnetic field is applied on the lattice, the energy becomes quantized into Landau levels which are different for the K and K' valleys when $0 < \alpha < 1$.

Recently, due to its exotic properties, the $\alpha - T_3$ model have been considered for valley filtering. Indeed, Hong-Ya Xu *et al.*²⁵ have used a geometric Valley Hall Effect in the $\alpha - T_3$ model as valley filtering. SK Firoz Islam *et al.*²⁶ have showed that the $\alpha - T_3$ model under a magnetic field acts as a valley filter when subjected to weak spatial electric and magnetic modulation.

We propose, in this paper, highly efficient valley filtering in the $\alpha - T_3$ model by using a combined electric and magnetic barrier. The electric barrier taken alone acts as a Fabry-Pérot interferometer where the particles can be transmitted across the barrier either by Klein tunneling or by Fabry-Pérot resonances that are analogous to those encountered in optics and the current crossing the electric barrier is not valley polarized. Adding the magnetic barrier to the electric barrier suppresses the Klein tunneling and induces valley-dependent Fabry-Pérot resonances which correspond to the Onsager semiclassical quantization of cyclotron orbits that coincide with the Landau levels. We also show that by considering a magnetic barrier alone, not only there is no valley-dependent transmission but also the transmission probability is almost the same for all the values of the parameter α .

The article is organized as follows. In Section II, we present the $\alpha - T_3$ model. Section III is devoted to cal-

culate the transmission probability, the conductivity and the polarization for the combined electric and magnetic barrier. In Section IV, our results are presented and the valley-dependent transmission is discussed. Finally, Section V, summarizes and concludes the present article.

II. PRESENTATION OF THE $\alpha - T_3$ MODEL

Graphene is a 2D layer of carbon atoms arranged in a HCL which results from the juxtaposition of regular hexagons. The crystallographic structure of graphene is then described by a triangular Bravais lattice whose primitive cell consists of two carbon atoms A and B because they are not equivalent from a crystallographic point of view.

Starting from the HCL of graphene and adding in the center of each hexagon an atom C connected to one of the two inequivalent sites (for example B) with a hopping amplitude $t_{BC} = t_{AB} = \frac{t}{\sqrt{2}}$ where t is the hopping amplitude between the sites A and B of HCL, we obtain the dice lattice T_3 ¹⁷.

The $\alpha - T_3$ model interpolates between HCL and dice lattice via the parameter α such as the hopping amplitudes are given by: $t_{BC} = \alpha t_{AB}$. Indeed, we obtain HCL for $\alpha = 0$ and the dice lattice for $\alpha = 1$. Fig. 1 shows the arrangement of the atoms within the $\alpha - T_3$ model. For computing convenience, we introduce the parameter φ such as $\tan \varphi = \alpha$.

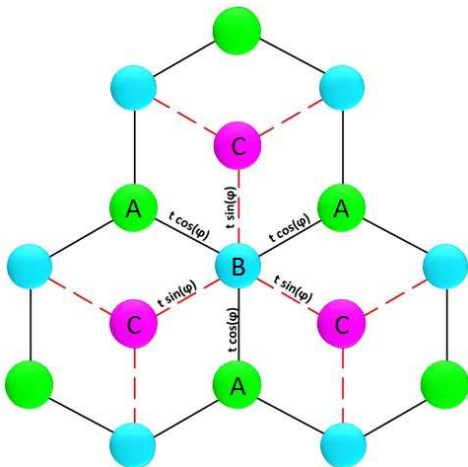


FIG. 1. (Color online) The $\alpha - T_3$ lattice. There are three sites A , B and C in each unit cell. The hopping amplitudes between the sites A and B are denoted $t \cos \varphi$ and those between the sites B and C are given by $t \sin \varphi$.

The low energy Hamiltonian for the $\alpha - T_3$ model can be written as:

$$H_o = \begin{pmatrix} 0 & f_o^\chi(k) \cos \varphi & 0 \\ f_o^{*\chi}(k) \cos \varphi & 0 & f_o^\chi(k) \sin \varphi \\ 0 & f_o^{*\chi}(k) \sin \varphi & 0 \end{pmatrix} \quad (1)$$

where $f_o^\chi(k) = \hbar v_F (\chi k_x - i k_y)$. Here $\chi = \pm 1$ is the valley index and v_F is the Fermi velocity. The spectrum consists of two cones whose energies are $E_s = s \hbar v_F |k|$ where $s = \pm$ refers to the band index and a flat band with energy $E = 0$. The corresponding wave functions are given by¹⁶:

$$\psi_s(\vec{r}) = \frac{1}{\sqrt{2}} \begin{pmatrix} \cos \varphi e^{i\theta_\chi} \\ s \\ \sin \varphi e^{-i\theta_\chi} \end{pmatrix} e^{i\vec{k}\vec{r}} \quad (2a)$$

$$\psi_0(\vec{r}) = \begin{pmatrix} \sin \varphi e^{i\theta_\chi} \\ 0 \\ -\cos \varphi e^{-i\theta_\chi} \end{pmatrix} e^{i\vec{k}\vec{r}} \quad (2b)$$

where $\theta_\chi = \arg f_o^\chi(k)$. The bands of the spectrum touch at the six corners of the Brillouin zone with two inequivalent points corresponding to the K and K' valleys (Fig. 2). We see from the expression of the energy that the band structure is independent of the parameter α whereas the eigenfunctions do.

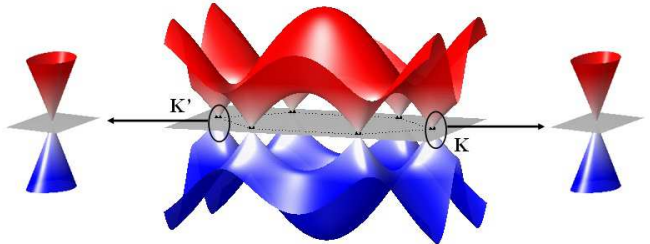


FIG. 2. (Color online) The energy spectrum of the $\alpha - T_3$ model consists of two dispersive bands and a flat band. The zoom-ins give the low energy spectrum around the K and K' valleys.

The $\alpha - T_3$ model is characterized by an α -dependent Berry phase that is continuously variable from π (for graphene) to 0 (for the dice lattice). The expression of the Berry phase is given respectively for the dispersive bands and for the flat band by¹⁶:

$$\theta_B = \chi \pi \cos 2\varphi \quad (3a)$$

$$\theta_{0B} = -\chi 2\pi \cos 2\varphi \quad (3b)$$

When subjected to a magnetic field, the energy becomes quantized, *i.e.* the electronic density is condensed into Landau levels. The energy of the Landau levels for the dispersive bands in the $\alpha - T_3$ model ($0 < \alpha < 1$) is different for the K and K' valleys and is given by :

$$\mathcal{E}_n^\chi = s \hbar \omega_c \sqrt{n + \frac{1}{2} - \frac{\chi}{2} \cos 2\varphi} \quad (4)$$

where $n = 0, 1, \dots$, the cyclotron pulsation is $\omega_c = \sqrt{2} \frac{v_F}{l_B}$ with $l_B = \sqrt{\frac{\hbar}{eB}}$ being the magnetic length.

The energy of the flat band remains zero. Note that for the graphene and the dice lattice, the Landau levels at the K and K' points are the same.

III. TUNNELING THROUGH AN ELECTRIC AND MAGNETIC BARRIER

Here we study the tunneling of Dirac fermions through a combined electric and magnetic barrier. The electric barrier $V(x)$ is of height V_0 and width L and the magnetic field $\vec{B}(x) = B(x)\vec{z}$ is perpendicular to the $\alpha - T_3$ lattice (Fig. 3) such as:

$$B(x) = B_0\Theta(x^2 - \frac{L^2}{4}) \quad (5a)$$

$$V(x) = V_0\Theta(x^2 - \frac{L^2}{4}) \quad (5b)$$

where Θ is the Heaviside step function.

In this case, the Hamiltonian reads:

$$H = \begin{pmatrix} V(x) & f^\chi(k) \cos \varphi & 0 \\ f^{*\chi}(k) \cos \varphi & V(x) & f^\chi(k) \sin \varphi \\ 0 & f^{*\chi}(k) \sin \varphi & V(x) \end{pmatrix} \quad (6)$$

where $f^\chi(k) = \chi\hbar v_F k_x - i(\hbar v_F k_y + e v_F A_y)$. Here A_y is the y component of the vector potential in the Landau gauge $\vec{A} = (0, A_y, 0)$ and its expression is given by:

$$A_y(x) = B_0 \begin{cases} -L/2 & \text{if } x < -L/2 \\ x & \text{if } |x| < L/2 \\ L/2 & \text{if } x > L/2 \end{cases} \quad (7)$$

The barrier is uniform along the y direction so that the y component of the wave vector is conserved. The wave function can thus be written as $\Phi(x, y) = \Psi(x) e^{ik_y y}$ where $\Psi(x) = (\psi_A(x), \psi_B(x), \psi_C(x))^T$ is the three-component pseudospinor.

By solving the Dirac equation $H\Psi(x) = E\Psi(x)$, we obtain the expression of the wave functions in the three regions of the barrier. In region I, the wave function is:

$$\Psi_I^\chi(x) = \frac{1}{\sqrt{2}} \begin{pmatrix} \chi e^{-i\chi\theta} \cos \varphi \\ 1 \\ \chi e^{i\chi\theta} \sin \varphi \end{pmatrix} e^{ik_x x} - \frac{r_\chi}{\sqrt{2}} \begin{pmatrix} \chi e^{i\chi\theta} \cos \varphi \\ -1 \\ \chi e^{-i\chi\theta} \sin \varphi \end{pmatrix} e^{-ik_x x} \quad (8)$$

The first and second terms refer respectively to the incident and reflected waves with the reflexion amplitude r_χ for the valley χ . The wave function in region III is given by:

$$\Psi_{III}^\chi(x) = \frac{t_\chi}{\sqrt{2}} \begin{pmatrix} \chi e^{-i\chi\theta'} \cos \varphi \\ 1 \\ \chi e^{i\chi\theta'} \sin \varphi \end{pmatrix} e^{iq_x x} \quad (9)$$

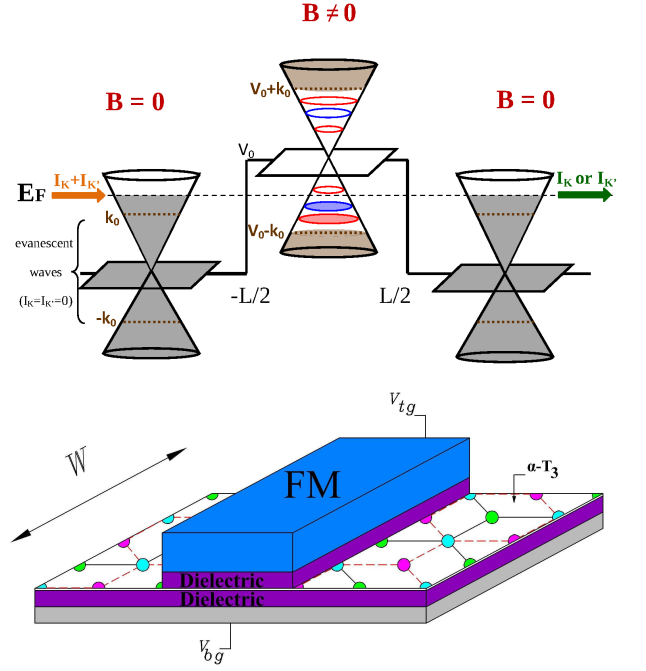


FIG. 3. (Color online) Top panel: Schematic of the spectrum in the $\alpha - T_3$ model tunneling through an electric and magnetic barrier. Outside the barrier, the occupied states are depicted in grey. Inside the barrier, the energy is quantized into Landau levels which are different for the K valley (red) and K' valley (blue) when $0 < \alpha < 1$. The orange and green arrows represent respectively the current injection ($I_K + I_{K'}$) and the valley polarized current (I_K or $I_{K'}$) for energies $E > k_0$. For energies $-k_0 < E < k_0$ there is no current due to evanescent waves. Here k_0 is given by Eq. (12). Bottom panel: Schematic of a combined electric and magnetic barrier produced by a ferromagnetic metallic (FM) strip deposited on the central region of the sample, a back gate potential V_{bg} and a top gate potential V_{tg} . V_{bg} and V_{tg} control respectively the Fermi energy E_F and the barrier height. The $\alpha - T_3$ sample is placed between two dielectric layers (purple strips).

where t_χ corresponds to the transmission amplitude for the χ valley. The incidence and the emergence angles are respectively written as:

$$\theta = \arctan\left(\frac{k_y - k_0}{k_x}\right) \quad (10)$$

$$\theta' = \arctan\left(\frac{k_y + k_0}{q_x}\right)$$

The wave vectors in the first and third regions read respectively:

$$k_x = \sqrt{E^2 - (k_y - k_0)^2} \quad (11)$$

$$q_x = \sqrt{E^2 - (k_y + k_0)^2}$$

where

$$k_o = \frac{\gamma L}{2} \quad (12)$$

with $\gamma = (\frac{L}{l_B})^2$. We used the following dimensionless variables: $E \rightarrow \frac{E}{t}$, $V_0 \rightarrow \frac{V_0}{t}$, $k_{xy} \rightarrow k_{xy}l$, $q_x \rightarrow q_x l$, $L \rightarrow \frac{L}{t}$ and $x \rightarrow \frac{x}{t}$ with $l = \frac{\hbar v_F}{t}$ and $l_B = \sqrt{\frac{\hbar}{eB}}$ is the magnetic length.

Inside the barrier, the wave functions for the K and K' valleys for $E \neq V_0$ are of the form:

$$\Psi_{II}^K(x) = a \begin{pmatrix} p_+ D_{p_+-1}(X) \cos \varphi \\ \lambda D_{p_+}(X) \\ -D_{p_++1}(X) \sin \varphi \end{pmatrix} + b \begin{pmatrix} -p_+ D_{p_+-1}(-X) \cos \varphi \\ \lambda D_{p_+}(-X) \\ D_{p_++1}(-X) \sin \varphi \end{pmatrix} \quad (13a)$$

$$\Psi_{II}^{K'}(x) = a \begin{pmatrix} D_{p_+-1}(X) \cos \varphi \\ \lambda D_{p_-}(X) \\ -p_- D_{p_--1}(X) \sin \varphi \end{pmatrix} + b \begin{pmatrix} -D_{p_+-1}(-X) \cos \varphi \\ \lambda D_{p_-}(-X) \\ p_- D_{p_--1}(-X) \sin \varphi \end{pmatrix} \quad (13b)$$

For $E = V_0$ and $\varphi \neq 0$, *i.e.* at the flat band, the wave functions become:

$$\Psi_{0II}^K(x) = a \begin{pmatrix} (p_+ + 1) D_{p_+-1}(X) \sin \varphi \\ 0 \\ D_{p_++1}(X) \cos \varphi \end{pmatrix} + b \begin{pmatrix} (p_+ + 1) D_{p_+-1}(-X) \sin \varphi \\ 0 \\ D_{p_++1}(-X) \cos \varphi \end{pmatrix} \quad (14a)$$

$$\Psi_{0II}^{K'}(x) = a \begin{pmatrix} D_{p_+-1}(X) \sin \varphi \\ 0 \\ (p_- + 1) D_{p_--1}(X) \cos \varphi \end{pmatrix} + b \begin{pmatrix} D_{p_+-1}(-X) \sin \varphi \\ 0 \\ (p_- + 1) D_{p_--1}(-X) \cos \varphi \end{pmatrix} \quad (14b)$$

where $\lambda = \frac{i(E-V_0)}{\sqrt{2\gamma}}$ and $X = \sqrt{\frac{2}{\gamma}}(k_y + \gamma x)$. Those latter wave functions are written using the parabolic cylinder functions D_{p_χ} ²⁷ of order p_χ given by:

$$p_\chi = \frac{1}{2} \left(\frac{(E - V_0)^2}{\gamma} + \chi \cos 2\varphi - 1 \right) \quad (15)$$

The matching conditions for particles in the $\alpha - T_3$ model²¹ are different from Schrödinger and Dirac particles. For that, we integrate the eigenvalue equation $H\Psi(x) = E\Psi(x)$ over the interval $[x_o - \eta, x_o + \eta]$ by taking $k_x = -i\frac{\partial}{\partial x}$ and we

find: $[S_x^\varphi \Psi(x_o + \eta) - S_x^\varphi \Psi(x_o - \eta)] = \int_{x_o - \eta}^{x_o + \eta} i\chi [(E - V(x))I_3 - (k_y + \gamma A(x))S_y^\varphi]$ where I_3 is the identity matrix, $S_x^\varphi = \begin{pmatrix} 0 & \cos \varphi & 0 \\ \cos \varphi & 0 & \sin \varphi \\ 0 & \sin \varphi & 0 \end{pmatrix}$ and $S_y^\varphi = i \begin{pmatrix} 0 & -\cos \varphi & 0 \\ \cos \varphi & 0 & -\sin \varphi \\ 0 & \sin \varphi & 0 \end{pmatrix}$. Sending η to 0, the second member of this latter equation vanishes, which leads to the matching conditions at x_o :

$$S_x^\varphi \Psi(x_o^+) = S_x^\varphi \Psi(x_o^-) \quad (16)$$

By using these boundary conditions for $x = \pm \frac{L}{2}$, we get the transmission amplitude t_χ . Details of the calculation are given in Appendix A.

To calculate the transmission probability we need to introduce the probability current²¹:

$$\vec{J} = \begin{cases} J_x = v_F (Re[\psi_B^* (\cos \varphi \psi_A + \sin \varphi \psi_C)]) \\ J_y = v_F (Im[\psi_B^* (\cos \varphi \psi_A - \sin \varphi \psi_C)]) \end{cases} \quad (17)$$

We finally end up with the transmission probability for the χ valley:

$$T_\chi = \frac{|J_x^{tr}|}{|J_x^{inc}|} = \left| \frac{\cos \theta'}{\cos \theta} \right| |t_\chi|^2 \quad (18)$$

where J_x^{tr} and J_x^{inc} are the transmitted and incident components of the current along the x direction which are calculated respectively from the first term of the wave function in region I (Eq. (8)) and the wave function in region III (Eq. (9)).

The transmission probability can be appreciated by using measurable quantities such as the conductivity which is given by employing the Landauer-Büttiker formula²⁸:

$$\sigma_\chi = \frac{L}{W} \frac{2e^2}{\hbar} \sum_{k_y} T_\chi(k_y) \quad (19)$$

Here W corresponds to the width of the barrier in the y direction. The factor 2 accounts for the spin degeneracy.

Finally, to better appreciate the difference between the K and K' valleys, it is judicious to calculate the valley polarization that is determined by:

$$P = \frac{\sigma_+ - \sigma_-}{\sigma_+ + \sigma_-} \quad (20)$$

It is important to note that particles can tunnel through the barrier, with a transmission probability given by Eq. (18), only if the wave vectors k_x and q_x (Eq. (11)) of the incident and transmitted waves are real which leads to $|E| > k_0$ and $k_0 - E < k_y < E - k_0$ as depicted in the blue zone in Fig. 5. However, for $|E| < k_0$ particles cannot travel the barrier because at

least one of the wave vectors k_x and q_x is imaginary. Particularly, when $E - k_0 < k_y < k_0 - E$ and $|E| < k_0$ (red zone in Fig. 5), both wave vectors q_x and k_x are imaginary and in this case the spectrum inside the pure magnetic barrier becomes quantized²⁹. In order to get the spectrum of the bound states, we consider the Dirac equation $H\Psi(x) = E\Psi(x)$ that leads to the Schrödinger equation for the second component $\psi_B(x)$ of the wave function $\Psi(x)$:

$$-\partial_x^2 \psi_B(x) + U(x)\psi_B(x) = E^2 \psi_B(x) \quad (21)$$

where the effective potential reads:

$$U(x) = \begin{cases} (k_y - k_0)^2 & x < -L/2 \\ (k_y + \gamma x)^2 + U_\chi & |x| < L/2 \\ (k_y + k_0)^2 & x > L/2 \end{cases} \quad (22)$$

with:

$$U_\chi = -\chi\gamma \cos 2\varphi \quad (23)$$

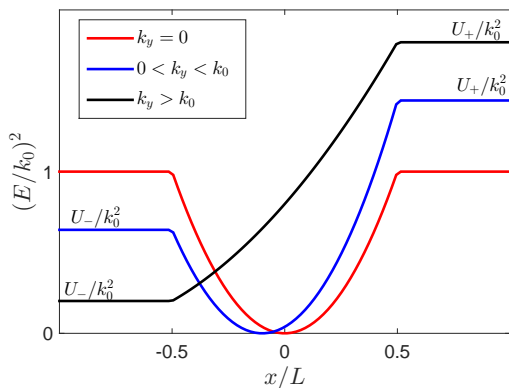


FIG. 4. (Color online) Potential $U(x)$ as a function of x for different values of $k_y \geq 0$ in the case where $U_\chi = 0$. For $k_y = 0$ (red line): symmetric quantum well of depth k_0^2 . For $0 < k_y < k_0$ (blue line): asymmetric quantum well of depth $U_- = (k_y - k_0)^2$. For $k_y > k_0$ (black line): there are no bound states. The expression of U_+ is given by $U_+ = (k_y + k_0)^2$.

We plot in Fig. 4, the potential $U(x)$ as a function of x for different values of k_y in the case where $U_\chi = 0$. The potential $U(x)$ represents a quantum well for $0 \leq k_y < k_0$ (blue and red lines) and thus the spectrum is quantized when $E - k_0 < k_y < k_0 - E$ and $|E| < k_0$ (red zone in Fig. 5). Otherwise, there are no bound states for $k_y \geq k_0$. Note that there is a maximum of bound states in the case of the symmetric quantum well ($k_y = 0$). If we take into account the term U_χ the spectrum inside the magnetic barrier is shifted upwards (downwards) for the K' (K) and this shift is responsible for the lifting of the valley degeneracy of the bound states of the barrier when $0 < \alpha < 1$. Hence, the spectrum corresponds approximately to the Landau levels³⁰ given by Eq. (4) as calculated in

the Appendix B.

The presence of the electric barrier ($V(x) \neq 0$) enables to shift upwards the spectrum by V_0 such as the progressive waves find inside the barrier the bound states (see Fig. 3) which leads to a valley dependent transmission and that is the aim of this work. However, the pure magnetic barrier ($V(x) = 0$) is not sufficient to obtain a valley-dependent transmission. Indeed, particles traveling the barrier ($|E| > k_0$) will find inside the barrier a continuum spectrum that does not enable to have a valley-dependent transmission as depicted in Fig. 5.

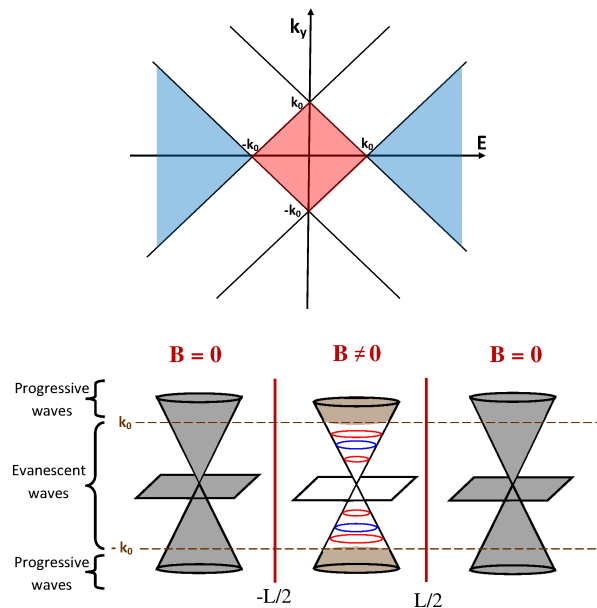


FIG. 5. (Color online) Top panel: Schematic representation in the (k_y, E) space of the two zones where the waves are evanescent (red zone with k_x and q_x imaginary) and are progressive (blue zone with k_x and q_x real). Lower panel: Schematic of the spectrum across a pure magnetic barrier in the $\alpha - T_3$ model. For $|E| < k_0$ no transmission is allowed due to the evanescent waves. For $|E| > k_0$, the particle can travel the barrier in which there is a continuum spectrum.

In order to make an optimal study of the transmission probability, we also take into consideration the potential barrier in the absence of magnetic field. In that case, the wave functions outside the barrier are given from Eq. (8) and Eq. (9) by taking the magnetic field $B = 0$. Inside the barrier, the wave function for $E \neq V_0$ becomes:

$$\Psi_{II} = \frac{a}{\sqrt{2}} \begin{pmatrix} e^{-i\Phi} \cos\varphi \\ s \\ e^{i\Phi} \sin\varphi \end{pmatrix} e^{iq_0 x} + \frac{b}{\sqrt{2}} \begin{pmatrix} -e^{i\Phi} \cos\varphi \\ s \\ -e^{-i\Phi} \sin\varphi \end{pmatrix} e^{-iq_0 x} \quad (24)$$

where $\Phi = \arctan\left(\frac{k_y}{q_0}\right)$, $q_0 = \sqrt{(E - V_0)^2 - k_y^2}$ and $s = \text{sign}(E - V_0)$.

For $E = V_0$, the Schrodinger equation $H\Psi(x) = E\Psi(x)$ gives:

$$\begin{cases} \cos \varphi (\partial_x + k_y) \psi_B(x) = 0 \\ \cos \varphi (\partial_x - k_y) \psi_A(x) + \sin \varphi (\partial_x + k_y) \psi_C(x) = 0 \\ \sin \varphi (\partial_x - k_y) \psi_B(x) = 0 \end{cases} \quad (25)$$

The solutions depend on either $k_y = 0$ or $k_y \neq 0$:

(i) for $k_y = 0$ and $\varphi \neq 0$, the wave function is a

constant: $\Psi_{0II}^{k_y=0}(x) = \begin{pmatrix} a \\ b \\ c \end{pmatrix}$.

(ii) for $k_y \neq 0$ and $\varphi \neq 0$, the wave function is given by:

$$\Psi_{0II}^{k_y \neq 0}(x) = \begin{pmatrix} ae^{k_y x} \\ 0 \\ be^{-k_y x} \end{pmatrix}.$$

We obtain the same wave functions for $0 < \alpha \leq 1$ as those obtained by Urban *et al.*²² for $\alpha = 1$. Hence, the transmission probability is given by: $\begin{cases} T(k_y = 0) = 1 \\ T(k_y \neq 0) = 0 \end{cases}$ as depicted in Fig. 6.

By using the matching conditions (Eq. (16)), we obtain the transmission probability in the absence of a magnetic field which is the same for the two valleys:

$$T_o = \frac{1}{1 + \frac{4\gamma_+\gamma_-}{(\gamma_+ - \gamma_-)^2} \sin^2(q_0 L)} \quad (26)$$

where

$$\gamma_{\pm} = (\cos \theta \mp s \cos \Phi)^2 + \cos^2 2\varphi (\sin \theta - s \sin \Phi)^2 \quad (27)$$

Here θ is given by Eq. (10) in the absence of the magnetic field ($B = 0$). This expression of the transmission probability is in coordination with the result found by E. Illes *et al.*²¹.

IV. RESULTS AND DISCUSSION

First of all, we focus on the case of a pure electric barrier. For that, we plot in Fig. 6 the transmission probability T_o , given by Eq. (26), as a function of the transverse momentum k_y and the energy E for different values of the parameter α . From the expression of the transmission probability given by Eq. (26), perfect transmission ($T_o = 1$) occurs when $\gamma_+\gamma_- = 0$ or $\sin^2(q_0 L) = 0$. The first case, known as the Klein tunneling effect²⁰, is available at normal incidence ($k_y = 0$) and for all values of the parameter α ²¹ and it is related to the conservation of the pseudospin. The second case implies $q_0 L = n\pi$ and it corresponds to the Fabry-Pérot resonances that are analogous to those encountered in optics. Fig. 6 (c) also points up a significant behavior for the dice lattice of

the transmission probability for an energy $E = \frac{V_0}{2}$: there is a perfect transmission for all values of the incidence angle and the barrier acts as if it was fully transparent and this is the so-called super Klein tunneling²². Indeed, in this case, the parameter γ_- given by Eq. (27) vanishes for all the values of k_y leading to a perfect transmission ($T_o = 1$). This figure also spotlights the fact that the transparency of the barrier enhances when the parameter α increases²¹. It is important to retain that the transmission probability is exactly the same for the K and K' valleys for all the values of the parameter α in the presence of an electric barrier.

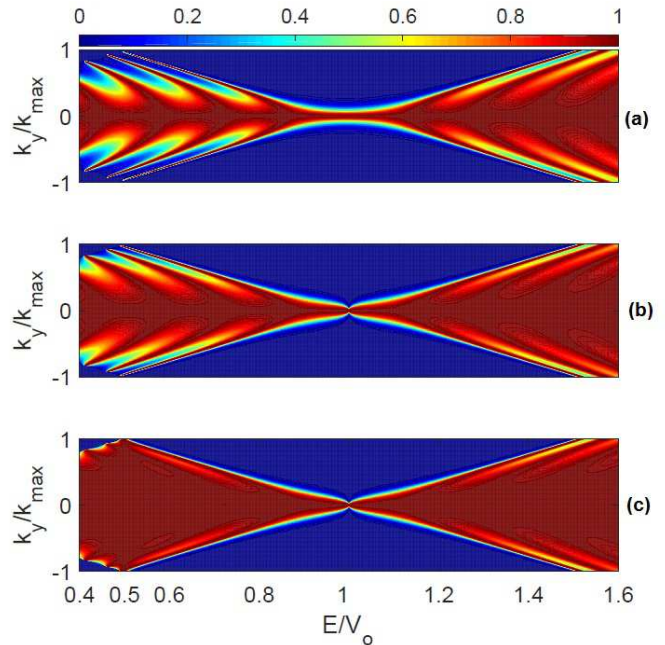


FIG. 6. (Color online) Transmission probability T_o (Eq. (26)) of the $\alpha - T_3$ model through an electric barrier of width $L = 450l$ and height $V_0 = 0.05t$ when $B = 0T$ as a function of the transverse momentum k_y and the energy for different values of the parameter α . (a) $\alpha = 0$ (HCL), (b) $\alpha = \frac{1}{\sqrt{3}}$ and (c) $\alpha = 1$ (dice lattice). The value of k_y must be taken such as the value of k_x (Eq. (11)) is real: $|k_y| < k_{max} = E$.

Then we take into consideration the tunneling through only a magnetic barrier. For that, we depicted in Fig. 7 the polar plot of the transmission probability for a parameter $\alpha = \frac{1}{\sqrt{3}}$ through a magnetic barrier as a function of the incident angle for different values of the barrier width L and the energy E . In this case, the transmission probability is given in Appendix A in the absence of the electric barrier ($V_o = 0$).

To interpret these results, we use the semiclassical approximation where the particle describes a cyclotron orbit of radius $r_c = \frac{|E|}{\gamma}$ ³¹ inside the magnetic barrier. The emergence of the particle at the second interface of the barrier depends on the incident angle θ , the cyclotron radius r_c and the width of the barrier L . Using the conservation of the transverse momentum k_y and from Eq.

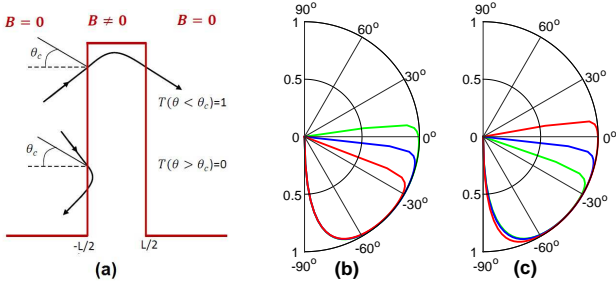


FIG. 7. (Color online) (a) Illustration of semiclassical trajectories of particles through a magnetic barrier for $\theta < \theta_c$ and $\theta > \theta_c$ where θ_c is the critical incident angle given by Eq. (28). (b-c) Polar plot of the transmission probability for a parameter $\alpha = 1/\sqrt{3}$ through a magnetic barrier ($B = 1T$) as a function of the incidence angle for different values of the barrier width L (b) and different values of the energy E (c). In panel (b), the energy is taken $E = 0.03t$ and the green line corresponds to $L = 350l$, the blue line is $L = 450l$ and the red line corresponds to $L = 550l$. In panel (c), the barrier width is taken $L = 450l$, the green line is $E = 0.026t$, the blue line is $E = 0.03t$ and the red one corresponds to $E = 0.04t$.

(10), we obtain the relation: $\sin \theta' = \sin \theta + \frac{2k_0}{E}$. We see from this relation that the transmission probability vanishes for all the incidence angles θ for the energies $|E| < k_0$ due to evanescent waves as discussed above and depicted in Fig. 5 (red zone).

In the case where $|E| > k_0$, the particle can emerge if $-1 < \sin \theta + \frac{2k_0}{E} < 1$ which implies that:

$$\sin \theta < 1 - \frac{2k_0}{E} = \sin \theta_c \quad (28)$$

where θ_c is the critical incident angle. Consequently, if $\theta < \theta_c$ (blue zone in Fig. 5), there is a perfect transmission while when $\theta > \theta_c$, the particle makes a full turn and is reflected as illustrated in Fig. 7(a) and hence the magnetic barrier in the $\alpha - T_3$ model confines the Dirac Weyl quasiparticles as in the case of graphene²⁴ and the dice lattice²². Thus, when considering only a magnetic barrier, the transmission is independent of the parameter α as mentioned by Urban *et al.*²² for the limiting cases (graphene and dice lattice).

We clearly see that for a given energy (Fig. 7(b)) when we increase the width of the magnetic barrier, the critical angle (Eq. (28)) decreases leading to a diminution of the transmission probability. In Fig. 7(c), we notice that for a given L the transmission probability increases when the energy enhances. We note that the transmission probability is exactly the same for the K and K' valleys in the case of the presence of only a magnetic barrier for all the values of the parameter α .

Let us now discuss the tunneling through a combined electric and magnetic barrier. To that end, we plot in Fig. 8 the transmission probability at the two valleys K and K' as a function of the transverse momentum k_y and the energy for different values of the parameter α . We notice first of all that the barrier becomes less transpar-

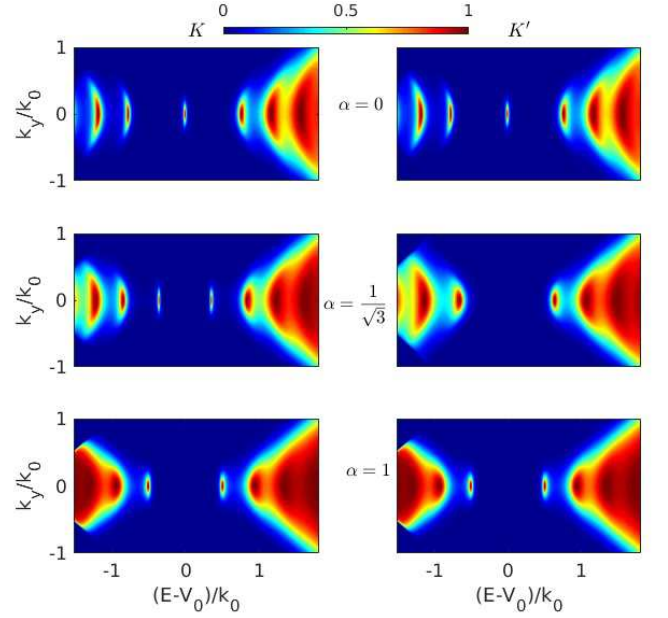


FIG. 8. (Color online) Transmission probability T_χ (Eq. (18)) for the two valleys K and K' through a combined electric and magnetic barrier as a function of transverse momentum k_y and the energy for the different values of the parameter α written in the figure. The parameters used here are: $V_0 = 0.05t$, $B = 1T$ and $L = 450l$.

ent in the presence of the magnetic field which is related to the fact that the electron exhibits, in a semiclassical picture, a circular orbit inside the barrier and the probability for the particle to reach the second interface of the barrier diminishes²⁹. Moreover, regardless of the value of the parameter α , there is a suppression of the Klein tunneling *i.e.* there is no perfect transmission at normal incidence ($k_y = 0$). In the case of the dice lattice ($\alpha = 1$), there is no more super Klein tunneling. For the HCL ($\alpha = 0$) and the dice lattice ($\alpha = 1$), *i.e.* the limiting cases of the $\alpha - T_3$ model, the transmission probability is identical for the valleys K and K' .

The main result of this article is seen for $0 < \alpha < 1$. Indeed, in Fig. 8 for $\alpha = \frac{1}{\sqrt{3}}$ the behavior of the transmission probability is different for K and K' which highlights a valley-dependent transmission. To better understand this behavior, we plot in Fig. 9 the transmission probabilities T_χ (full lines) for the two valleys K and K' at $k_y = 0$ as a function of the energy for the three same parameters α as used in Fig. 8. For $\alpha = 0$ and $\alpha = 1$ (Fig. 9), the transmission probabilities for the two valleys K and K' (plotted in black full lines) are exactly the same which brings out that the particle in those cases present no valley-dependent transmission. However, for $\alpha = \frac{1}{\sqrt{3}}$ the transmission probabilities for the two valleys are different as illustrated in Fig. 9 where the full red line corresponds to the transmission for the K valley and the full blue line refers to the K' valley. This last result is also available for all the values of α that

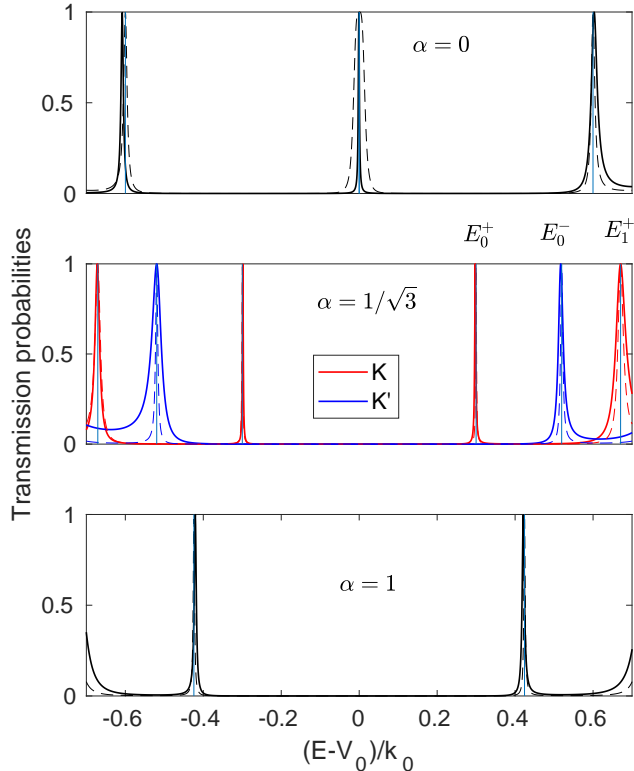


FIG. 9. (Color online) Transmission probability T_χ (Eq. (18)) (full lines) and transmission probability T_{FP}^χ (Eq. (31)) in the Fabry-Pérot form (dashed lines) at normal incidence ($k_y = 0$) through a combined electric and magnetic barrier as a function of the energy for different values of α ($\alpha = 0$, $\alpha = \frac{1}{\sqrt{3}}$ and $\alpha = 1$). The parameters used here are: $V_0 = 0.05t$, $B = 1.5T$ and $L = 450l$. The light blue vertical lines represent the Landau levels given by Eq. (4).

verify $0 < \alpha < 1$. This behavior can be understood in the semiclassical picture by the interference between the forward and backward waves inside the barrier. In this case, the longitudinal momentum depends on the x position and is given by $k_x = \sqrt{(E - V_0)^2 - \gamma^2 x^2}$ and when the cyclotron radius $r_c = \frac{|E - V_0|}{\gamma} < \frac{L}{2}$ we distinguish three regions as depicted in Fig. 10:

(i) when $-L/2 < x < -r_c$ and $r_c < x < L/2$: these are the classically forbidden regions where k_x is imaginary and the electron is transmitted through these regions with the probabilities in the WKB approximation³²: $t = t_1 = t_2 = \exp\left(-2\text{Im} \int_{r_c}^{L/2} k_x dx\right)$ which is given by the following form:

$$t = \exp\left[-\frac{(E - V_0)^2}{\gamma} \left(u\sqrt{u^2 - 1} - \log(u + \sqrt{u^2 - 1})\right)\right] \quad (29)$$

where $u = L/(2r_c)$.

(ii) when $-r_c < x < r_c$ the longitudinal momentum

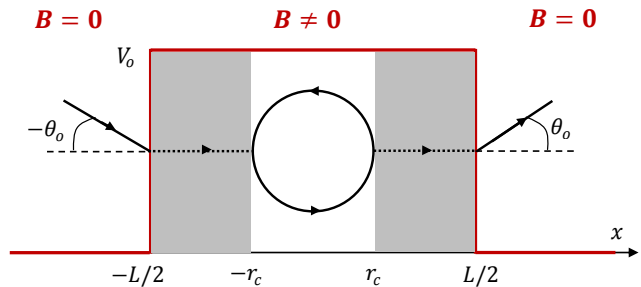


FIG. 10. (Color online) Illustration of the transmission probability at $k_y = 0$ through a combined electric and magnetic barrier in the semiclassical picture. The particles travel in the grey regions with evanescent waves while in the middle region ($-r_c < x < r_c$) they perform a cyclotron orbit. The angle $\theta_o = \arcsin \frac{k_o}{E}$ is calculated from Eq. (10) at $k_y = 0$.

k_x is real so the electron exhibits cyclotron orbits with radius r_c and the phase acquired from the interference of the wave scattered between the two classically forbidden region $x = \pm r_c$ is given by:

$$\Delta\theta = \theta_{WKB} + \theta_1 + \theta_2 + \theta_B \quad (30)$$

where $\theta_{WKB} = 2 \int_{-r_c}^{r_c} \sqrt{(E - V_0)^2 - \gamma^2 x^2} dx = \frac{(E - V_0)^2}{\gamma}$, $\theta_1 + \theta_2 = \pi$ are the backreflection phases for the interfaces 1 and 2³² and θ_B is the valley-dependent Berry phase given by Eq. (3a).

Using the values of the transmission coefficients t (Eq. (29)) and the phase $\Delta\theta$ (Eq. (30)), we can write the valley-dependent transmission probability in the Fabry-Pérot form:

$$T_\chi^{FP} = \frac{t^2}{|1 - (1 - t)e^{i\Delta\theta}|^2} \quad (31)$$

which is shown in Fig. 9 by the dashed lines.

We see from this figure that the perfect transmission $T_\chi^{FP} = 1$ in the Fabry-Pérot form occurs at the Landau levels E_n^χ (vertical lines). Indeed, this perfect transmission is obtained from the Onsager semiclassical quantization condition³¹ $\Delta\theta = 2n\pi$ with $n = 1, 2, \dots$ which is equivalent to Eq. (4) with $\mathcal{E}_n^\chi = E_n^\chi - V_0$. The transmission resonances $T_\chi = 1$ coincide perfectly with the Landau levels E_n^χ showing pronounced peaks when the cyclotron orbit is quite distant from the interfaces of the barrier. Otherwise, the transmission resonances deviate slightly from the Landau levels and become wider. This last result can be attributed to the effect of the walls at $\pm L/2$ on the cyclotron orbit. It changes the energy of the Landau levels in a manner similar to that of the quantum Hall edge channels³³. For this reason, we focus on the first Landau levels energies $E_0^\chi = \mathcal{E}_0^\chi + V_0$ (see Eq. (4)) at the K and K' valleys where $T_\chi \approx T_{FP}^\chi$ (see Fig. 9 for $\alpha = 1/\sqrt{3}$). The transmission probabilities centered around these Landau levels have a Lorentzian

distribution and the half width at half maximum is given by:

$$\Delta E_n^x = \frac{\gamma}{2(E_n^x - V_0)} \frac{t(E_n^x - V_0)}{\sqrt{1 - t(E_n^x - V_0)}} \approx \frac{\sqrt{\frac{\pi}{2}}}{2 \sin \varphi} e^{-\frac{\gamma L^2}{4}} \quad (32)$$

This energy width is small when either the magnetic field or the barrier width is large.

Moreover, the value of the parameter α must be chosen such as the overlap between the transmission probabilities around two neighboring Landau levels is minimal. For that, the Landau level E_0^- must be halfway between E_0^+ and E_1^+ (Fig. 9) which gives $(\cos \varphi - \sin \varphi) = \sqrt{1 + \sin^2 \varphi} - \cos \varphi$. This last result leads to $\varphi = 0,57$ which justifies our choice of $\varphi = \frac{\pi}{6}$ ($\alpha = \frac{1}{\sqrt{3}}$). Hence, by choosing the appropriate values of the Fermi energy, the parameter α , the magnetic field and the barrier width and height such as the ratio $r_c/(L/2)$ is as small as possible, we can get highly efficient valley-dependent transmission. The simultaneous presence of an electric and magnetic barrier in the $\alpha - T_3$ model with $0 < \alpha < 1$ can be thus used as valley filtering.

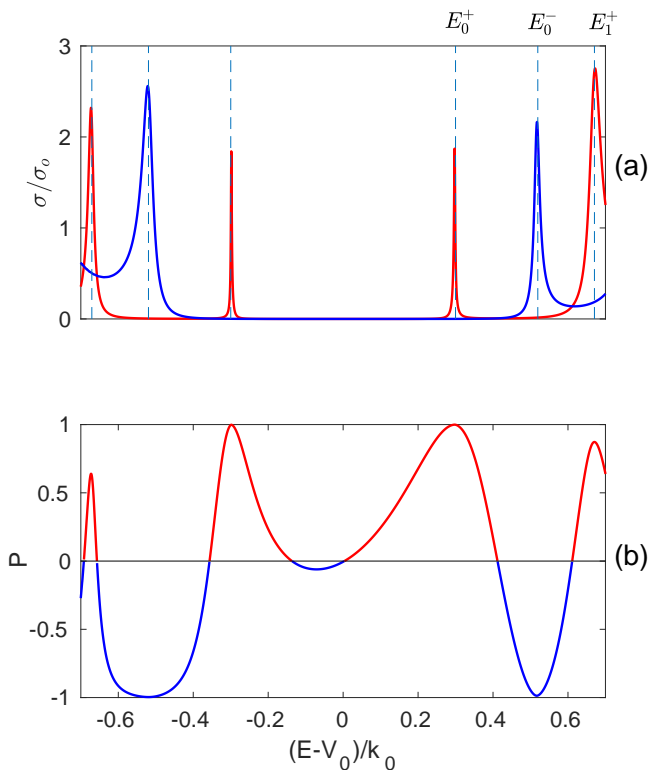


FIG. 11. (Color online)(a) Conductivity and (b) polarization for the combined electric and magnetic barrier as a function of the energy for $\alpha = \frac{1}{\sqrt{3}}$, $L = 450l$, $B = 1.5T$ and $V_0 = 0.05t$. The vertical light blue dashed lines in Fig. (a) represent the Landau levels given by Eq. (4).

Achieving a valley-dependent conductivity is easily fea-

sible experimentally compared to the transmission probability. For that, we plot in Fig. 11 the conductivity (Eq. (19)) and the polarization (Eq. (20)) as a function of the energy for the combined electric and magnetic barrier when $\alpha = \frac{1}{\sqrt{3}}$. In Fig. 11(a) the red line corresponds to the conductivity for the K valley and the blue one refers to the K' valley. We also note here that the Landau levels (vertical light blue dashed lines) corresponding to the quantized energy levels coincide perfectly with the peaks of conductivity of the K and K' valleys. For a value of Fermi energy equal to one of the Landau levels (for example for the K valley), the K component of the electrons pass through the barrier while those of the other valley are reflected. As seen in Fig. 11(b), the values taken by the polarization fluctuate between -1 and 1 so that $P = 1(-1)$ means that the out-coming current consists of only $K(K')$ contribution.

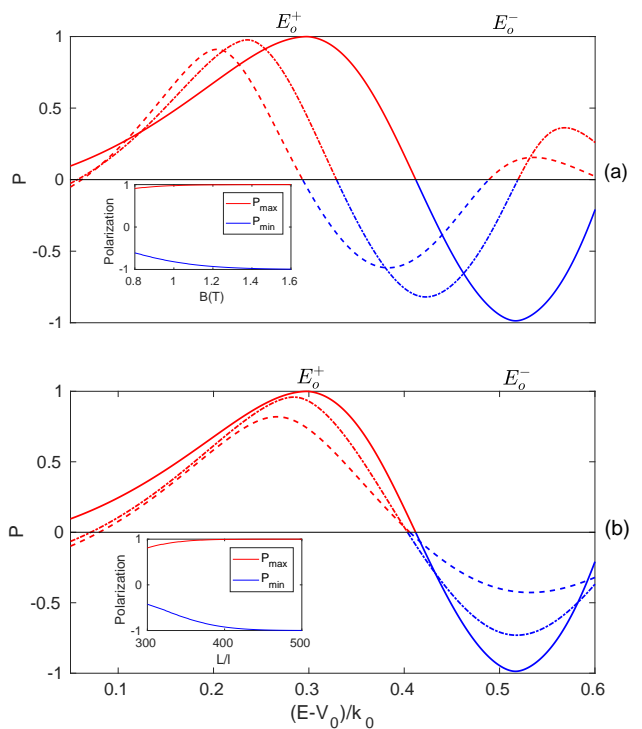


FIG. 12. (Color online) Polarization for the combined electric and magnetic barrier as a function of the energy for $\alpha = \frac{1}{\sqrt{3}}$. (a) For $L = 450l$, three different values of the magnetic field B were considered: $B = 0.8T$ (dashed line), $B = 1.0T$ (dotted line) and $B = 1.5T$ (full line). (b) For $B = 1.5T$, three different values of barrier width were taken: $L = 300l$ (dashed line), $L = 350l$ (dotted line) and $L = 450l$ (full line). The insets represent the maximum and minimum polarizations around the Landau level E_0^+ and E_0^- as a function of the magnetic field (a) and the barrier width (b). The value of the parameter k_0 , given by Eq. (12), is calculated with $B = 1.5T$ and $L = 450l$ as in Figs. 8, 9 and 11.

Fig. 12 shows the polarization, when $\alpha = \frac{1}{\sqrt{3}}$, for the electric and magnetic barrier as a function of the energy for different values of the magnetic field (a) and for dif-

ferent values of the barrier width (b). For a given barrier width as in Fig. 12(a), the polarization is improved by the enhancement of the magnetic field. The polarization can even become perfect for $B \geq 1.5T$, as seen in the inset, when $L = 450l$. Likewise, for a fixed magnetic field B , enhancing the width L increases the polarization as seen in Fig. 12(b). $L = 450l$ is required to reach full polarization as depicted in the inset. These results can be understood, as discussed previously, by the fact that to achieve a high valley polarization, there must be a minimal overlap between neighbouring Landau levels and the width at half maximum must be small which is feasible by enhancing L and/or B .

V. CONCLUSION

In summary, we studied a way to produce a valley polarized current using a combined magnetic and electric barrier in the $\alpha-T_3$ model. To obtain a valley-dependent transmission, three conditions are necessary:

- (i) the magnetic barrier to obtain the Landau levels.
- (ii) the electric barrier to shift upwards the spectrum such as the progressive waves find inside the barrier the bound states .
- (iii) $0 < \alpha < 1$ to lift the valley degeneracy between Landau levels.

Our results showed that perfect transmission ($T = 1$) through this kind of barrier occurs at the Landau levels by choosing the appropriate values of the magnetic field and the barrier width and height. In our model, the valley-dependent current traveling the barrier is tuned by the Fermi energy.

As an experimental realization, we propose to use the electric and magnetic barrier on the $Hg_{1-x}Cd_xTe$ at the critical doping $x = 0.17$ which maps onto the $\alpha - T_3$ model for a parameter $\alpha = \frac{1}{\sqrt{3}}$ as shown in Fig. 3. By tuning the Fermi energy controlled by the back gate voltage (V_{bg}), we can select the desired current. Such a valley filtering effect could be probed by using a polarizer/analyzer geometry, *i.e.* creating a second such barrier but well separated from the first one in order to avoid interferences between the two barriers.

ACKNOWLEDGMENTS

We would like to thank J.-N. Fuchs and F. Piéchon for invaluable help and fruitful discussions. We are also indebted to them for a critical reading of the manuscript. This work was partially supported by the Tunisian-French CMCU 15G1306 project.

Appendix A: The transmission amplitude

Applying the matching conditions (Eq. (16)) at $x = \pm \frac{L}{2}$ for the total wave function given from Eq. (8), Eq.

(9) and Eqs. (13a) and (13b), we obtain a system of four equations for each valley for $E \neq V_0$:

$$\begin{aligned} e^{-ik_x \frac{L}{2}} + r_\chi e^{ik_x \frac{L}{2}} &= a\lambda D_{p_\chi}(X_-) + b\lambda D_{p_\chi}(-X_-) \\ ue^{-ik_x \frac{L}{2}} - r_\chi \bar{u} e^{ik_x \frac{L}{2}} &= aF^\chi(X_-) - bF^\chi(-X_-) \\ t_\chi e^{iq_x \frac{L}{2}} &= a\lambda D_{p_\chi}(X_+) + b\lambda D_{p_\chi}(-X_+) \\ vt_\chi e^{iq_x \frac{L}{2}} &= aF^\chi(X_+) - bF^\chi(-X_+) \end{aligned} \quad (A1)$$

Straight forward, the transmission amplitude t_χ for the $K(\chi = 1)$ and $K'(\chi = -1)$ valleys is given by:

$$t_\chi = \frac{C}{x_1 x'_2 - x'_1 x_2} [x'_2 D_p(X_+) - x'_1 D_p(-X_+)] \quad (A2)$$

where we have used:

$$\begin{aligned} C &= \lambda(u + \bar{u})e^{-i(k_x - q_x)\frac{L}{2}} \\ u &= \chi [\cos^2 \varphi e^{-i\chi\theta} + \sin^2 \varphi e^{i\chi\theta}] \\ v &= \chi [\cos^2 \varphi e^{-i\chi\theta'} + \sin^2 \varphi e^{i\chi\theta'}] \\ x_1 &= \lambda \bar{u} D_p(X_-) + F^\chi(X_-) \\ x_2 &= \lambda \bar{u} D_p(-X_-) - F^\chi(X_+) \\ x'_1 &= \lambda v D_p(X_+) + F^\chi(X_+) \\ x'_2 &= \lambda v D_p(-X_+) + F^\chi(-X_+) \\ F^+(X) &= \cos^2 \varphi p_+ D_{p_+ - 1}(X) - \sin^2 \varphi D_{p_+ + 1}(X) \\ F^-(X) &= \sin^2 \varphi p_- D_{p_- - 1}(X) - \cos^2 \varphi D_{p_- + 1}(X) \end{aligned} \quad (A3)$$

with $X_\pm = \sqrt{\frac{2}{\gamma}}(k_y \pm k_0)$, $k_0 = \frac{\gamma L}{2}$, $\lambda = \frac{i(E - V_0)}{\sqrt{2\gamma}}$, θ and θ' are given by Eq. (10) and p_χ by Eq. (15). \bar{u} is the conjugate complex of u .

At the flat band in the central region for $E = V_0$ and $\varphi \neq 0$, by applying the matching conditions Eq. (16) at $x = \pm \frac{L}{2}$, the total wave functions given from Eqs. (8), (9), (14a) and (14b), we obtain a system of four equations for each valley:

$$\begin{aligned} e^{-ik_x \frac{L}{2}} + r_\chi^0 e^{ik_x \frac{L}{2}} &= 0 \\ ue^{-ik_x \frac{L}{2}} - r_\chi^0 \bar{u} e^{ik_x \frac{L}{2}} &= \frac{\sin 2\varphi}{2} [aG^\chi(X_-) + bG^\chi(-X_-)] \\ t_\chi^0 e^{-iq_x \frac{L}{2}} &= 0 \\ vt_\chi^0 e^{-iq_x \frac{L}{2}} &= \frac{\sin 2\varphi}{2} [aG^\chi(X_+) + bG^\chi(-X_+)] \end{aligned} \quad (A4)$$

where $G^\chi(X) = (p_\chi + 1)D_{p_\chi - 1}(X) + D_{p_\chi + 1}(X)$. Hence, the transmission amplitude is $t_\chi^0 = 0$.

Appendix B: Bound states in the magnetic barrier

From the Schrödinger equation (Eq. (21)), the wave function $\psi_B(x)$ in the three regions are given by:

$$\psi_B(x) = \begin{cases} ce^{k_x x}, & x < -L/2 \\ aD_{p_x}(X) + bD_{-1-p_x}(iX), & |x| < L/2 \\ de^{-q_x x}, & x > L/2 \end{cases} \quad (\text{B1})$$

where $k_x = \sqrt{(k_y - k_0)^2 - E^2}$, $q_x = \sqrt{(k_y + k_0)^2 - E^2}$, $X = \sqrt{\frac{2}{\gamma}}(k_y + \gamma x)$ and p_x is given by Eq. (15). The continuity of the function $\psi_B(x)$ and its derivative at $x = \pm L/2$ leads to a system of four equations for each valley:

$$\begin{aligned} ce^{k_x \frac{L}{2}} &= aD_{p_x}(X_-) + bD_{-1-p_x}(iX_-) \\ ck_x e^{k_x \frac{L}{2}} &= a\partial_x D_{p_x}(X_-) + b\partial_x D_{-1-p_x}(iX_-) \\ de^{-q_x \frac{L}{2}} &= aD_{p_x}(X_+) + bD_{-1-p_x}(iX_+) \\ -dq_x e^{-q_x \frac{L}{2}} &= a\partial_x D_{p_x}(X_+) + b\partial_x D_{-1-p_x}(iX_+) \end{aligned} \quad (\text{B2})$$

where $X_{\pm} = \sqrt{\frac{2}{\gamma}}(k_y \pm k_0)$. By setting to 0 the determinant of this system, we get the energies of the bound states inside the barrier for $|E| < k_0$ and $-k_0 + E <$

$k_y < k_0 - E$ as depicted in Fig. 13 as a function of the transverse momentum k_y .

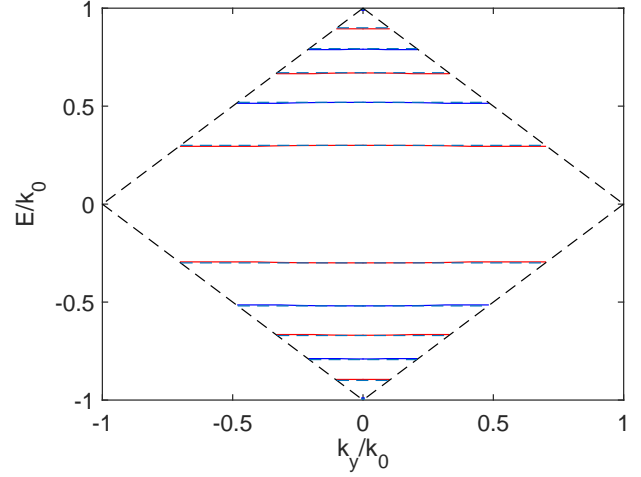


FIG. 13. (Color online) Energies of bound states as a function of k_y for $\alpha = \frac{1}{\sqrt{3}}$, $L = 450l$ and $B = 1.5T$. The red and blue continuous lines correspond respectively to the energies of the K and K' valleys. The horizontal light blue dashed lines represent the Landau levels given by Eq. (4).

* Electronic address: lassaad.mandhour@istmt.utm.tn

- ¹ J. R. Schaibley, H. Y. Yu, G. Clark, P. Rivera, J. S. Ross, K. L. Seyler, W. Yao, and X. D. Xu, Nat. Rev. Mater. **1**, 16055 (2016).
- ² A. Rycerz, J. Tworzydło, and C. W. J. Beenakker, Nature Phys. **3**, 172 (2007).
- ³ I. Zutic, J. Fabian, and S. Das Sarma, Rev. Mod. Phys. **76**, 323 (2004).
- ⁴ C. Yesilyurt, S.G. Tan, G. Liang, and M.B.A. Jalil, AIP Adv. **6**, 056303 (2016).
- ⁵ V. Hung Nguyen, S. Dechamps, P. Dollfus, and J.-C. Charlier, Phys. Rev. Lett. **117**, 247702 (2016).
- ⁶ D. Zhai and N. Sandler, Phys. Rev. B **98**, 165437 (2018).
- ⁷ T. Fujita, M. B. A. Jalil, and S. G. Tan, Appl. Phys. Lett. **97**, 043508 (2010).
- ⁸ F. Zhai, X. F. Zhao, K. Chang, and H. Q. Xu, Phys. Rev. B **82**, 115442 (2010).
- ⁹ S.-G. Cheng, J. Zhou, H. Jiang, and Q.-F. Sun, New J. Phys. **18**, 103024 (2016).
- ¹⁰ D. Gunlycke and C. T. White, Phys. Rev. Lett. **106**, 136806 (2011).
- ¹¹ J. M. Pereira Jr., F. M. Peeters, R. N. Costa Filho, and G. A. Farias, J. Phys.: Condens. Matter **21**, 045301 (2009).
- ¹² M. M. Asmar and S. E. Ulloa, Phys. Rev. B **96**, 201407 (2017).
- ¹³ J. J. Wang, S. Liu, J. Wang, and J. F. Liu, Sci. Rep. **7**, 10236 (2017).

- ¹⁴ Y. S. Ang, S. A. Yang, C. Zhang, Z. Ma, and L. K. Ang, Phys. Rev. B **96**, 245410 (2017).
- ¹⁵ C.-S. Park, Phys. Lett. A **382**, 121 (2017).
- ¹⁶ A. Raoux, M. Morigi, J.-N. Fuchs, F. Piéchon, and G. Montambaux, Phys. Rev. Lett. **112**, 026402 (2014).
- ¹⁷ B. Sutherland, Phys. Rev. B **34**, 5208 (1986).
- ¹⁸ J. Vidal, R. Mosseri and B. Douçot, Phys. Rev. Lett. **81**, 5888 (1998).
- ¹⁹ J. D. Malcolm and E. J. Nicol, Phys. Rev. B **92**, 035118 (2015).
- ²⁰ M. I. Katsnelson, K. S. Novoselov, and A. K. Geim, Nature Physics **2**, 620 (2006).
- ²¹ E. Illes and E. J. Nicol, Phys. Rev. B **95**, 235432 (2017).
- ²² D.F. Urban, D. Bercioux, M. Wimmer and W. Häusler, Phys. Rev. B **84**, 115136 (2011).
- ²³ Y. Li, Q. Wan, Y. Peng, G. Wang, Z. Qian, G. Zhou, and M. B. A. Jalil, Scientific Reports **5**, 18458 (2015).
- ²⁴ A. De Martino, L. Dell'Anna, and R. Egger, Phys. Rev. Lett. **98**, 066802 (2007).
- ²⁵ H.-Y. Xu, L. Huang, D. Huang, and Y.-C. Lai, Physical Review B **96**, 045412 (2017).
- ²⁶ S. F. Islam and P. Dutta, Phys. Rev. B **96**, 045418 (2017).
- ²⁷ I. S. Gradshteyn and I. M. Ryzhik, Table of Integrals, Series, and Product (Academic Press, Inc., New York, 1980).
- ²⁸ Ya. M. Blanter and M. Büttiker, Phys. Rep. **336**, 1 (2000).
- ²⁹ M. Ramezani Masir, P. Vasilopoulos and F. M. Peeters,

- Phys. Rev. B **82**, 115417 (2010).
- ³⁰ M. Ramezani Masir, P. Vasilopoulos, A. Matulis, and F. M. Peeters, Phys. Rev. B **77**, 235443 (2008).
- ³¹ J.N. Fuchs, F. Piéchon, M.O. Goerbig, and G. Montambaux, Eur. Phys. J. B **77**, 351 (2010).
- ³² A. V. Shytov, M. S. Rudner, and L. S. Levitov, Phys. Rev. Lett. **101**, 156804 (2008).
- ³³ B.I. Halperin, Phys. Rev. B **25**, 2185 (1982).